The Astronomical Journal, 146:95 (10pp), 2013 October doi:10.1088/0004-6256/146/4/95
© 2013. The American Astronomical Society. All rights reserved. Printed in the U.S.A.

SPIN STATE AND MOMENT OF INERTIA CHARACTERIZATION OF 4179 TOUTATIS

Yu Takahashi[1,3], Michael W. Busch[2,4], and D. J. Scheeres[1,5]
[1] University of Colorado at Boulder, 429 UCB, Boulder, CO 80309-0429, USA
[2] National Radio Astronomy Observatory, 1003 Lopezville Road, Box O, Socorro, NM 87801, USA
Received 2013 May 17; accepted 2013 August 6; published 2013 September 12

ABSTRACT

The 4.5 km long near-Earth asteroid 4179 Toutatis has made close Earth flybys approximately every four years between 1992 and 2012, and has been observed with high-resolution radar imaging during each approach. Its most recent Earth flyby in 2012 December was observed extensively at the Goldstone and Very Large Array radar telescopes. In this paper, Toutatis' spin state dynamics are estimated from observations of five flybys between 1992 and 2008. Observations were used to fit Toutatis' spin state dynamics in a least-squares sense, with the solar and terrestrial tidal torques incorporated in the dynamical model. The estimated parameters are Toutatis' Euler angles, angular velocity, moments of inertia, and the center-of-mass–center-of-figure offset. The spin state dynamics as well as the uncertainties of the Euler angles and angular velocity of the converged solution are then propagated to 2012 December in order to compare the dynamical model to the most recent Toutatis observations. The same technique of rotational dynamics estimation can be applied to any other tumbling body, given sufficiently accurate observations.

Key words: minor planets, asteroids: individual (Toutatis) – planets and satellites: dynamical evolution and stability – planets and satellites: interiors

1. INTRODUCTION

The 4.5 km long near-Earth asteroid 4179 Toutatis (hereafter Toutatis) is close to a 4:1 orbital resonance with the Earth, and has made six close Earth flybys since its discovery in 1989 (Ostro et al. 1999). The first radar imaging campaigns of Toutatis in 1992 and 1996 were led by Ostro and Hudson with the Arecibo Planetary Radar and the Goldstone Solar System Radar, and their results revealed a tumbling, non-principal axis (NPA) rotator with a two-lobed shape (Ostro et al. 1995, 1999; Hudson & Ostro 1995, 1998; Hudson et al. 2003; Spencer et al. 1995), as shown in Figure 1.

Hudson & Ostro (1995) discussed that Toutatis' tumbling rotation could be described as a 5.41 day spin period around its long axis with a precession period of 7.35 days around the asteroid's angular momentum vector. Scheeres et al. (2000) showed that Toutatis' current NPA spin state is consistent with the history of close flybys between the asteroid and the Earth. This NPA rotation mode becomes an advantage when estimating, or at least constraining, the internal mass distribution of the body. The NPA rotation mode is a complex function of the initial spin state (i.e., orientation and angular velocity) and moments of inertia. The moments of inertia are functions of the mass distribution of the body, so their values put a strong constraint on the mass and density distribution of the body. Such a constraint cannot be enforced on a principal-axis rotator simply by looking at its rotation mode, as its spin state only depends on the rotation axis and the rotation period. That is, its rotational dynamics do not depend on the mass distribution.

In this paper, Toutatis' moment of inertia ratios are estimated using the radar images captured with the Arecibo Planetary Radar and the Goldstone Solar System Radar from 1992 to 2008. These observations are fit in a least-squares sense to accurately model the rotational dynamics, incorporating solar and terrestrial tidal torques. Specifically, Euler angles, angular velocity, moment of inertia ratios, and the center-of-mass–center-of-figure (COM-COF) offset of the body are included in the state vector to be estimated. It is of particular interest to estimate the moment of inertia ratios (i.e., I_{ij}/I_{zz}, which is the ratio of the ij component of the inertia tensor to I_{zz}) and the COM-COF offset, as these values constrain the internal density distribution of the body. Our estimation of these parameters was performed prior to the 2012 December apparition, and predictions from our model are compared with the actual data collected then.

The results show that Toutatis' moment of inertia ratios are known to within a few percent, and Toutatis' predicted orientation fits the actual 2012 observations within the formal uncertainty of 20–30 deg for each of the 3-1-3 Euler angles. This is the first time that an Earth-crossing asteroid's spin state has been estimated to this precision from ground observations. The Toutatis shape model is being updated with the most recent radar images, and the estimated moment of inertia ratios and the COM-COF offset will be used to constrain the internal density distribution of the body in the future.

2. ROTATIONAL DYNAMICS

The motion of a rotating rigid body is reviewed in this section. Most of the equations are discussed in detail by Schaub & Junkins (2009), and only the key equations are presented here.

2.1. Euler Angles

An inertial frame and a body-fixed frame can be related via the rotation matrix composed of the 3-1-3 Euler angles $\boldsymbol{\alpha}=(\alpha, \beta, \gamma)$, as shown in Figure 2.

The body frame is obtained by rotating the body z-axis by α, then the body x-axis by β, and finally the body z-axis by γ, all measured positive in the counterclockwise direction when

[3] PhD, Aerospace Engineering Sciences, University of Colorado at Boulder, 429 UCB, Boulder, CO 80309-0429, USA.
[4] Jansky Fellow, National Radio Astronomy Observatory, 1003 Lopezville Road, Box O, Socorro, NM 87801, USA.
[5] A. Richard Seebass Endowed Chair Professor, Aerospace Engineering Sciences, University of Colorado at Boulder, 429 UCB, Boulder, CO 80309-0429, USA.

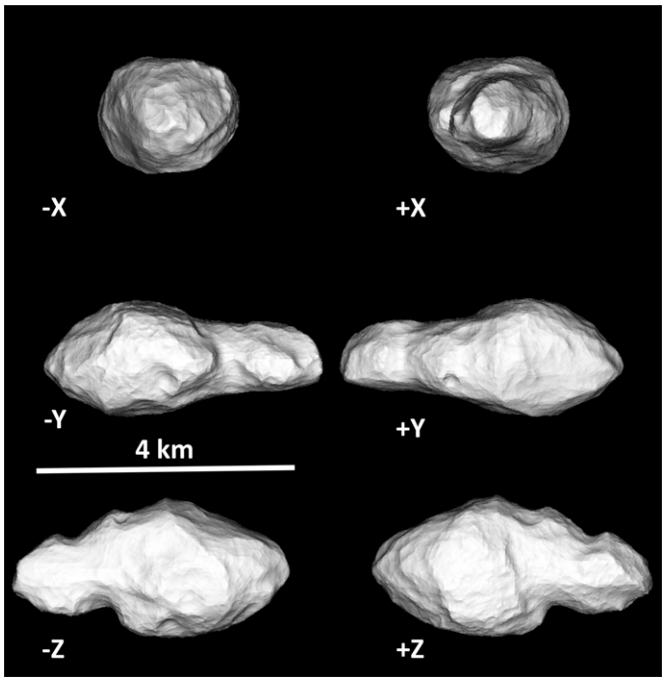

Figure 1. Toutatis shape model, refined from that of Hudson et al. (2003) and viewed from along its principal axes. The x-, y-, and z-axes are the long, intermediate, and short principal axes, respectively. The model is based on the 1992–2008 images only.

looking down into the axis of rotation. Using the Euler angles, the rotation matrix $[BN]$ that maps a vector from the inertial frame to the body frame is given as

$$[BN] = \mathscr{R}_{3,\gamma} \cdot \mathscr{R}_{1,\beta} \cdot \mathscr{R}_{3,\alpha}, \tag{1}$$

where $\mathscr{R}$ is the rotation matrix with the subscript indicating the axis of rotation (i.e., $x \rightarrow 1$, $y \rightarrow 2$, and $z \rightarrow 3$) and the angle of rotation (θ) as follows:

$$\mathscr{R}_{1,\theta} = \begin{bmatrix} 1 & 0 & 0 \\ 0 & \cos\theta & \sin\theta \\ 0 & -\sin\theta & \cos\theta \end{bmatrix}; \tag{2}$$

$$\mathscr{R}_{3,\theta} = \begin{bmatrix} \cos\theta & \sin\theta & 0 \\ -\sin\theta & \cos\theta & 0 \\ 0 & 0 & 1 \end{bmatrix}. \tag{3}$$

Thus, the Euler angles are direct measures of the orientation of a rigid body in the inertial frame, which motivates expressing their dynamical equations in order to relate a set of Euler angles at one epoch to that at another. Without proof, the time derivative of the 3-1-3 Euler angles, $\boldsymbol{\alpha}$, is given by the following equation:

$$\dot{\boldsymbol{\alpha}} = \frac{1}{\sin\beta} \begin{bmatrix} \sin\gamma & \cos\gamma & 0 \\ \cos\gamma\sin\beta & -\sin\gamma\sin\beta & 0 \\ -\sin\gamma\cos\beta & -\cos\gamma\cos\beta & \sin\beta \end{bmatrix} \times \boldsymbol{\omega}_B = [C(\boldsymbol{\alpha})]\boldsymbol{\omega}_B, \tag{4}$$

where $\boldsymbol{\omega}$ is the angular velocity. Note that the angular velocity must be expressed in the body frame, as indicated by the B subscript. Equation (4) suffers a singularity when $\beta = 0$ deg or 180 deg because the first and third rotation axes are aligned in these two cases. These conditions were never encountered for the whole duration of Toutatis' rotational dynamics propagation.

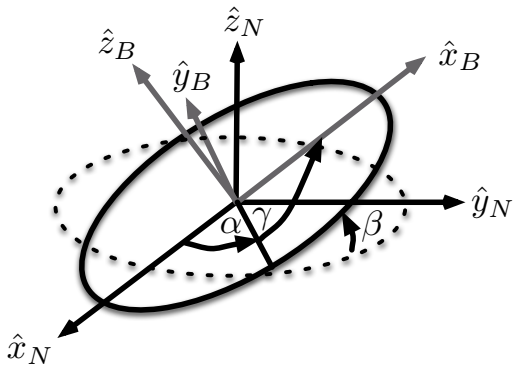

Figure 2. Euler Angles and inertia/body coordinate frames. The N subscript is used for the inertial coordinate frame and the B subscript for the body coordinate frame, both of which are defined by a set of three orthonormal, right-handed vectors $\hat{x}$, $\hat{y}$, and $\hat{z}$.

The rotation matrix $[BN]$ becomes useful when computing the torques due to the Earth and Sun, as the orbit of a planet is generally expressed in the inertial frame but the torque computation must be performed in the body frame. The torque computation and orbit propagation method are discussed in Sections 2.3 and 3, respectively.

2.2. Angular Velocity

The time derivative of the angular velocity is computed by Euler's equation. In order to derive the equation, the angular momentum around the center of mass is defined as

$$\boldsymbol{H}_{\mathrm{CM}} = I_{\mathrm{CM}}\boldsymbol{\omega}_{\mathrm{CM}}, \tag{5}$$

where the inertia tensor I_{CM} is a constant, symmetric $[3 \times 3]$ tensor in the body frame and can be defined by six independent quantities. Then, the rate of change of the angular momentum around the center of mass in the body frame is related to the torque ($\boldsymbol{L}_{B,\mathrm{CM}}$) acting on the system as follows:

$$\dot{\boldsymbol{H}}_{B,\mathrm{CM}} = I_{B,\mathrm{CM}}\dot{\boldsymbol{\omega}}_{B,\mathrm{CM}} + [\tilde{\omega}_{B,\mathrm{CM}}]I_{B,\mathrm{CM}}\boldsymbol{\omega}_{B,\mathrm{CM}} = \boldsymbol{L}_{B,\mathrm{CM}}, \tag{6}$$

where the tilde denotes the cross-product operator defined as

$$[\tilde{\omega}] = \begin{bmatrix} 0 & -\omega_3 & \omega_2 \\ \omega_3 & 0 & -\omega_1 \\ -\omega_2 & \omega_1 & 0 \end{bmatrix}. \tag{7}$$

By rearranging Equation (6), Euler's equation is obtained:

$$\dot{\boldsymbol{\omega}}_{B,\mathrm{CM}} = I^{-1}_{B,\mathrm{CM}}(-[\tilde{\omega}_{B,\mathrm{CM}}]I_{B,\mathrm{CM}}\boldsymbol{\omega}_{B,\mathrm{CM}} + \boldsymbol{L}_{B,\mathrm{CM}}). \tag{8}$$

The computation of the external torque is discussed in the next section.

2.3. External Torque

The external torque $\boldsymbol{L}_{B,\mathrm{CM}}$ in the body frame about the center of mass of a rigid body due to an external spherical mass can be modeled as

$$\boldsymbol{L}_{B,\mathrm{CM}} = -M_s\boldsymbol{r} \times \frac{\partial U}{\partial \boldsymbol{r}}, \tag{9}$$

where

$$U = G\int_M \frac{dm(\boldsymbol{r}')}{|\boldsymbol{r} - \boldsymbol{r}'|}. \tag{10}$$

In Equation (9), U is the potential due to the rigid body, M is the mass of the rigid body, M_s is the mass of the spherical body, $\boldsymbol{r}$ is the position of the spherical body relative to the rigid body, and the prime is used to denote the quantities of a mass element (dm) within the rigid body. Thus, in order to compute the external torque properly, it is necessary to know the gravity field of the rigid body (i.e., density distribution) and the relative position between the rigid body and the sphere. The computation of the relative position is deferred to Section 3, and the potential expression is studied in this section.

The gravity potential in Equation (10) is expressed in the spherical harmonic expansion as

$$U = \frac{GM^*}{R^*}\sum_{n=0}^{\infty}\sum_{m=0}^{n}\left(\frac{R^*}{r}\right)^{n+1} P_{nm}(\sin\phi) \cdot \begin{bmatrix}\cos(m\lambda)\\ \sin(m\lambda)\end{bmatrix}\cdot\begin{bmatrix}C_{nm}\\ S_{nm}\end{bmatrix}, \tag{11}$$

where G is the gravitational constant, M^* and R^* are the reference mass and reference radius, P_{nm} is the associated Legendre function of degree n and order m, ϕ and λ are the latitude and longitude of the spherical body in the body frame, and C and S are the spherical harmonic coefficients defined as

$$\begin{cases} C_{nm} = \dfrac{(2-\delta_{0,m})}{M^*}\dfrac{(n-m)!}{(n+m)!}\displaystyle\int_M\left(\frac{r'}{R^*}\right)^n \\ \quad \times P_{nm}(\sin\phi')\cos(m\lambda')dm', \\ S_{nm} \overset{m>0}{=} \dfrac{2}{M^*}\dfrac{(n-m)!}{(n+m)!}\displaystyle\int_M\left(\frac{r'}{R^*}\right)^n \\ \quad \times P_{nm}(\sin\phi')\sin(m\lambda')dm', \end{cases} \tag{12}$$

where δ is the Kronecker delta function. By direct expansion, the first- and second-degree spherical harmonic coefficients are shown to be functions of the COM-COF offset and the moments of inertia as follows:

$$\begin{cases} R^*C_{11} = x_{\mathrm{CM}}, \\ R^*S_{11} = y_{\mathrm{CM}}, \\ R^*C_{10} = z_{\mathrm{CM}}; \end{cases} \tag{13}$$

$$\begin{cases} C_{20} = \dfrac{1}{2M^*(R^*)^2}(I_{xx}+I_{yy}-2I_{zz}), \\ C_{21} = -\dfrac{1}{M^*(R^*)^2}I_{xz}, \\ C_{22} = \dfrac{1}{4M^*(R^*)^2}(I_{yy}-I_{xx}), \\ S_{21} = -\dfrac{1}{M^*(R^*)^2}I_{yz}, \\ S_{22} = -\dfrac{1}{2M^*(R^*)^2}I_{xy}. \end{cases} \tag{14}$$

Thus, as shown in Equation (9), the COM-COF offset and the moment of inertia ratios give rise to the perturbations by the external torques through the first- and second-degree gravity coefficients. In so many words, the observations (i.e., Euler angles discussed in Section 4) are related to the rotational dynamics in Equation (8), enabling one to process their information to estimate the COM-COF offset and the moment of inertia ratios. Only a $[2\times 2]$ gravity field is used to compute the terrestrial and solar tidal torques, as the third-degree gravity perturbations are proven to be negligible in the preliminary analysis.

Now that the general torque computation is discussed, the gravity potential and acceleration of the first- and second-degree spherical harmonic coefficients can be solved explicitly. The first-degree potential is expressed as

$$U_1 = \frac{GM^*}{r^3}\boldsymbol{r}\cdot\boldsymbol{r}_{\mathrm{CM}}, \tag{15}$$

which yields

$$\frac{\partial U_1}{\partial \boldsymbol{r}} = \frac{GM^*}{r^3}[1_{[3\times 3]} - 3\hat{r}\hat{r}]\cdot\boldsymbol{r}_{\mathrm{CM}} = \frac{GM^*R^*}{r^3}[1_{[3\times 3]} - 3\hat{r}\hat{r}]\cdot\begin{bmatrix}C_{11}\\ S_{11}\\ C_{10}\end{bmatrix}. \tag{16}$$

Thus, the acceleration due to the COM-COF offset is a linear function of itself. Substitution of Equation (16) into Equation (9) yields the torque due to the first-degree spherical harmonic coefficients as

$$\boldsymbol{L}_1 = -M_s\boldsymbol{r}\times\frac{\partial U_1}{\partial\boldsymbol{r}} = -\frac{GM^*M_s}{r^3}[\tilde{r}]\cdot\boldsymbol{r}_{\mathrm{CM}} = -\frac{GM^*M_sR^*}{r^3}[\tilde{r}]\cdot\begin{bmatrix}C_{11}\\ S_{11}\\ C_{10}\end{bmatrix}. \tag{17}$$

In addition, the second-degree potential is defined as

$$U_2 = \frac{G}{2r^3}I_T - \frac{3G}{2r^5}\boldsymbol{r}\cdot[I]\cdot\boldsymbol{r}, \tag{18}$$

where I_T is the trace of the inertia tensor. Note that $\boldsymbol{r}\cdot[I]\cdot\boldsymbol{r}$ is tensorial notation, which yields a scalar and should not be confused with the dot product of vectors. Then, the acceleration due to the second-degree potential becomes

$$\frac{\partial U_2}{\partial\boldsymbol{r}} = -\frac{3G}{2r^5}I_T\boldsymbol{r} + \frac{15G}{2r^7}(\boldsymbol{r}\cdot[I]\cdot\boldsymbol{r})\boldsymbol{r} - \frac{3G}{r^5}[I]\boldsymbol{r}, \tag{19}$$

which yields

$$\boldsymbol{L}_2 = \frac{3GM_s}{r^5}[\tilde{r}][I]\boldsymbol{r}. \tag{20}$$

Significant external torques on Toutatis are exerted by both the Earth and Sun. These separate contributions must be summed together.

3. TOUTATIS' ORBIT

Toutatis is nearly in a 4:1 resonance with the Earth, in an eccentric, low-inclination orbit. Figure 3 shows the heliocentric orbit of Toutatis (black) and Earth (gray) in the inertial J2000 frame.

The observations, to be discussed in the next section, were taken between 1992 and 2012 during either the inbound or outbound leg of the Earth crossings. Table 1 shows the observation

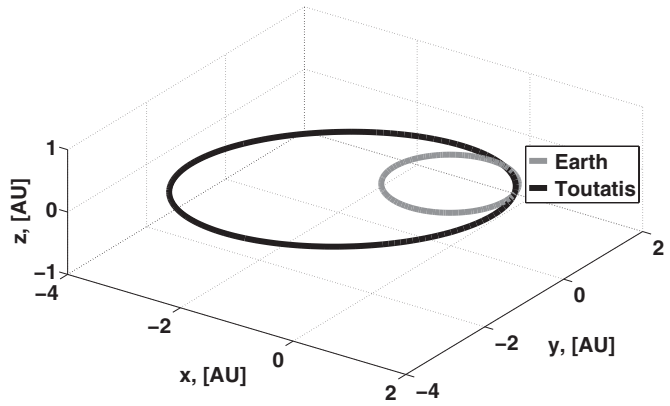

Figure 3. Toutatis' orbit. The semi-major axis is $a = 2.53$ [AU], the eccentricity is $e = 0.629$ (n.d.), and the inclination is $i = 0.446$ (deg).

epochs and the minimum distance from the Earth to Toutatis during these periods.

Toutatis' closest approach to Earth since its discovery occurred during the 2004 flyby, at a distance of four lunar distances, and the recent flyby in 2012 December will be the closest Earth encounter between then and 2069. During the outbound leg of the 2012 December flyby, Toutatis was imaged by the Chinese Chang'e 2 spacecraft, a lunar probe that departed from the Earth–Moon L2 Lagrange point to fly by Toutatis as an extended mission. This was the first time that a near-Earth asteroid has flown by a spacecraft while making a flyby of Earth.

As shown in Figure 3, the Earth apparition nearly coincides with the perihelion passage when the torque due to the solar tide becomes the greatest. In order to illustrate the significance of the Earth flybys and solar tidal torque on the change in the rotation dynamics of the asteroid, Figure 4 shows the signed change in the magnitude of the angular momentum, normalized by the initial angular momentum magnitude at a reference epoch in 1992.

Figure 4 shows that the solar tide exerts a strong torque around perihelion passage, and the terrestrial tidal torques further change the rotation dynamics of Toutatis (0.1% change in the magnitude of the angular momentum in 20 yr). The terrestrial tide is significant only during each Earth flyby, so the dynamical model only includes it from one month before until one month after each flyby epoch. The solar tide is active at all times, and tides from the Moon are proven to be negligible (≈1% of the terrestrial tides). Although the magnitude of the angular momentum is relatively constant between each Earth flyby, there are small oscillations due to the solar tide that lead to significant orientation offsets. The 2004 apparition is by far the strongest perturbation from the terrestrial tides, as indicated by a large change in the magnitude of the angular momentum.

Table 1
Observation Epochs and Earth–Toutatis Distance

Year	Month	$D_{\min}$ (Lunar Distance)
1992	November	9.40
1996	November	13.79
2000	October	28.75
2004	September	4.03
2008	November	19.56
2012	December	18.03

Not only the rotation dynamics, but also Toutatis' orbit changes due to perturbations after every Earth flyby and during the course of its heliocentric orbit, which prohibits one from using simple two-body dynamics in the heliocentric frame. Therefore, Toutatis' orbit was retrieved from the JPL Horizons system (http://ssd.jpl.nasa.gov/?horizons). The relative position of Toutatis with respect to Earth was obtained in 30 minute increments, and that of Toutatis with respect to the Sun was obtained in one-day increments. The terrestrial torques were computed by linearly interpolating Toutatis' position in the inertial frame. For the solar tidal torque, a more accurate interpolation method, the f–g series (Danby 1962, chapter 6.7), was employed due to the large time interval in order to lower the position errors to less than ∼10 [m].

4. OBSERVATIONS

The fundamental observational data used in our estimation were obtained by correlating radar images of Toutatis to the existing shape model. For example, Figure 5 shows the delay-Doppler radar images of Toutatis from Goldstone in 2000 and Arecibo in 2004 and 2008.

Within each image in Figure 5, time delay, equivalent to distance from the Earth, increases from top to bottom, and Doppler frequency, equivalent to line-of-sight velocity, increases from left to right. These images have a total range extent of 5 km, and a range resolution of 18.75 m pixel^{-1} at Goldstone and 15 m pixel^{-1} at Arecibo. The Doppler extents of the images

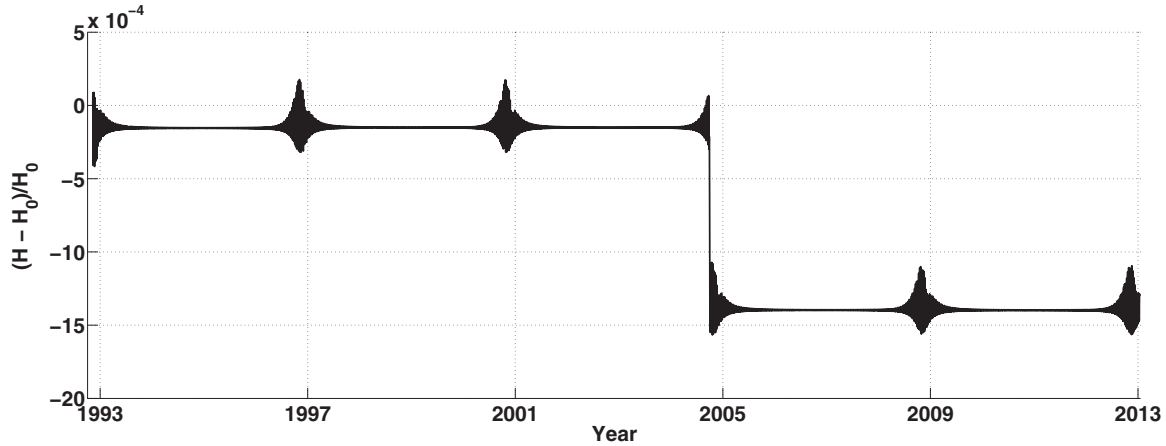

Figure 4. Change in Toutatis' rotational angular momentum magnitude H over time.

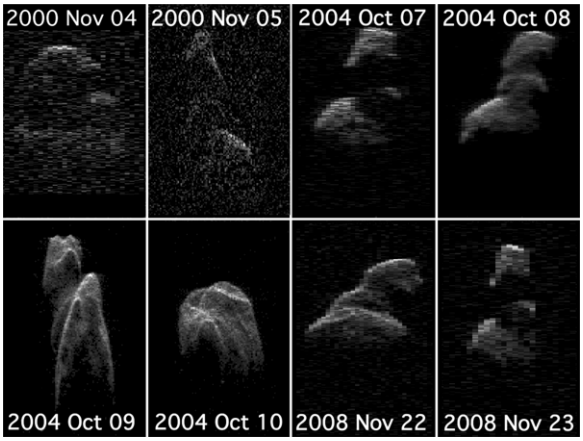

Figure 5. Delay-Doppler radar images of Toutatis from Goldstone in 2000 and Arecibo in 2004 and 2008.

vary; Doppler resolution was 0.033 Hz at Goldstone, 0.011 Hz at Arecibo in 2004, and 0.019 Hz at Arecibo in 2008. In this projection, Toutatis appears to rotate counterclockwise, but because of the asteroid's slow rotation, there is little rotation smear during the imaging during each day. The Goldstone images have low signal-to-noise ratios because of the greater distance to the asteroid in 2000 and the relatively low sensitivity of the telescope as compared to Arecibo.

Using these radar images, the 3-1-3 Euler angles, along with the body frame angular velocity, were estimated at each observation epoch. All observations are listed in Table 3 in Appendix A.2. There are varying numbers of observations for each apparition, totaling 17 observations in 1992, 8 observations in 1996, 2 observations in 2000, 4 observations in 2004, and 2 observations in 2008. Uncertainties have been omitted for brevity, but range between 3 deg and 15 deg for Euler angles and between 2 deg day^{-1} and 10 deg day^{-1} for components of the instantaneous spin vectors. These observations were processed by the filter (Section 5) to estimate the rotational dynamics and relevant physical parameters of Toutatis. Another example of the radar images is presented in Figure 6.

Figure 6 shows the predicted orientation of Toutatis on 2008 November 23 using the best-fit torque-free spin state for the 2000–2004 images (left) compared to the observed orientation (center). The ~100 deg offset in the asteroid's orientation is due to the tidal torques, primarily from the Earth during the 2004 flyby. Including the terrestrial torque resolves the discrepancy (right). Insets show the orientation of the Toutatis shape model projected onto the plane of the sky for the two spin state models. Arecibo viewed Toutatis nearly end-on, with the smaller lobe closer to Earth. The observed and modeled radar images are oriented as in Figure 5.

5. LEAST-SQUARES FILTER

All of the 1992–2008 Euler angle observations were fit in a least-squares sense incorporating both terrestrial and solar tidal torques. For this purpose, a batch filter with a square-root information filter algorithm was implemented, and observations were processed with respect to the epoch (i.e., t_0) to get the best estimates of the epoch state. The estimated quantities are the initial Euler angles, angular velocity, moment of inertia ratios, and a potential COM-COF offset. This section briefly reviews the filter equations for the least-squares batch filter. Most of the

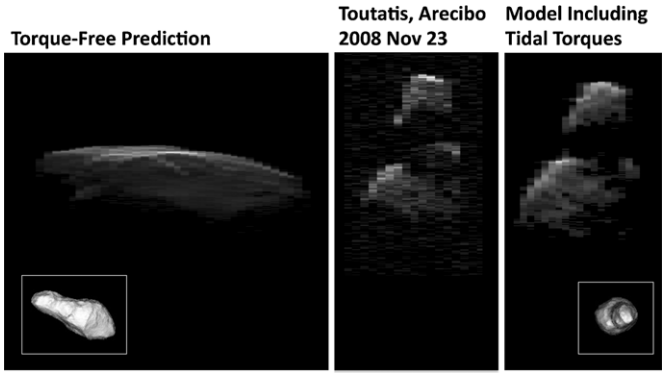

Figure 6. Predicted orientation of Toutatis on 2008 November 23.

equations in this section are well documented by Tapley et al. (2004), and only the key steps are highlighted.

5.1. Dynamical Equations

For a state vector $\boldsymbol{X}$ that is an array of estimated parameters, we have the dynamical equation $\dot{\boldsymbol{X}}$ and observation $\boldsymbol{Y}$:

$$\dot{\boldsymbol{X}} = F(\boldsymbol{X}, t); \tag{21}$$

$$\boldsymbol{Y}_k = Z(\boldsymbol{X}_k, t_k) + \boldsymbol{\epsilon}_k, \tag{22}$$

where F is the dynamical equation that computes the time derivative of the state vector, Z is the observation model, $\boldsymbol{\epsilon}$ is the observation error, and k is the index of the time t. As mentioned above, the state vector consists of the 3-1-3 Euler angles, angular velocity, moment of inertia ratios, and COM-COF offset:

$$\boldsymbol{X} = [\boldsymbol{\alpha} \quad \boldsymbol{\omega}_B \quad \bar{I} \quad \bar{\boldsymbol{r}}], \tag{23}$$

where $\boldsymbol{\alpha}$ is the 3-1-3 Euler angles in a vector form, $\boldsymbol{\omega}$ is the angular velocity with the B subscript indicating the body frame notation, $\bar{I}$ is an array of moment of inertia ratios, and $\bar{\boldsymbol{r}}$ is the COM-COF offset. As the dynamical equation is non-linear for a rotating rigid body, it is only possible to estimate the corrections to the full state. Assuming that the dynamics of the reference state stays sufficiently close to the true state over the period of data arc, Equations (21) and (22) can be expanded in a first-order Taylor series to yield

$$\dot{\boldsymbol{x}}(t) = A(t)\boldsymbol{x}(t); \tag{24}$$

$$\boldsymbol{y}_k = \tilde{H}_k \boldsymbol{x}_k + \boldsymbol{\epsilon}_k. \tag{25}$$

This process is often called the "linearization" of the dynamical and observable equations. In Equations (24) and (25), lowercase letters are used to denote the deviations of the full state, A is the dynamics matrix, and $\tilde{H}$ is the observation partial given as

$$A(t) = \left.\frac{\partial F(t)}{\partial \boldsymbol{X}(t)}\right|_{\boldsymbol{X}=\boldsymbol{X}^*}; \tag{26}$$

$$\tilde{H}_k = \left.\frac{\partial Z}{\partial \boldsymbol{X}}\right|_{\boldsymbol{X}=\boldsymbol{X}^*(t_k)}, \tag{27}$$

where $\boldsymbol{X}^*$ is the reference state. Thus, both the dynamics matrix and the observation partial are computed on the reference

trajectory, and the state deviation follows the dynamics dictated by Equation (26). As the observables are the 3-1-3 Euler angles, the observation partial yields a simple form:

$$\tilde{H}_k = [1_{[3\times3]} \quad 0_{[3\times11]}]. \tag{28}$$

Now, we realize that the linearized observation equation (Equation (25)) only relates the state deviation at time t_k to the observation deviation at the same time. If we were to estimate all state deviations at different times, the number of observations is generally much smaller than the number of estimated parameters, yielding an underdetermined system. In order to avoid this rank-deficiency, the state deviation at $t = t_k$ is mapped back to epoch ($t = t_0$) so the observation made at time $t = t_k$ can be related to the state deviation at $t = t_0$. Such reformulation can be achieved by introducing the state transition matrix (STM), which is expressed as

$$\Phi(t_2, t_1) = \frac{\partial \boldsymbol{X}(t_2)}{\partial \boldsymbol{X}(t_1)}. \tag{29}$$

That is, the STM is the partial of the state at time t_2 with respect to the state at time t_1. Or rather, it can be rephrased as the sensitivity of the state at $t = t_1$ to the state at $t = t_2$. Then, this STM can be used to map the state deviation from time t_1 to time t_2 as follows:

$$\boldsymbol{x}(t_2) = \Phi(t_2, t_1)\boldsymbol{x}(t_1). \tag{30}$$

This property of the STM is of great importance, as it allows one to relate the observation deviation at time $t = t_k$ to the state deviation at epoch as follows:

$$\boldsymbol{y}_k = \tilde{H}_k \boldsymbol{x}_k + \boldsymbol{\epsilon}_k = \tilde{H}_k \Phi(t_k, t_0)\boldsymbol{x}_0 + \boldsymbol{\epsilon}_k = H_k \boldsymbol{x}_0 + \boldsymbol{\epsilon}_k, \tag{31}$$

where $H_k = \tilde{H}_k \Phi(t_k, t_0)$. The significance of Equation (31) is subtle but important. Equation (31) states that the state deviation at $t = t_k$ can be mapped back to epoch t_0 with the use of the STM. That is, the state deviation at epoch t_0 has sensitivity to the observation made at $t = t_k$. Thus, the information in observations at future times can be mapped back and accumulated with respect to epoch t_0, allowing one to solve for the epoch time state deviation.

For a system of non-linear dynamical equations, the STM cannot be computed analytically and has to be numerically propagated together with the reference state. The time derivative of the STM is given as

$$\dot{\Phi}(t, t_0) = A(t)\Phi(t, t_0), \tag{32}$$

where $\Phi(t_0, t_0)$ is the identity matrix by definition. The computation of the dynamics matrix A is described in Appendix A.1.

5.2. Cost Function

The goal of a least-squares filter is to minimize the cost function J defined as

$$J = \frac{1}{2}(\boldsymbol{y} - H\boldsymbol{x}_0)^T W(\boldsymbol{y} - H\boldsymbol{x}_0) + \frac{1}{2}(\bar{\boldsymbol{x}}_0 - \boldsymbol{x}_0)^T \bar{P}_0^{-1}(\bar{\boldsymbol{x}}_0 - \boldsymbol{x}_0), \tag{33}$$

where W is the observation weighting matrix, P is the covariance matrix, and barred quantities are a priori values. Specifically, $\bar{P}_0$ is the a priori covariance matrix of the estimated parameters at $t = t_0$. Then, this cost function is differentiated with respect to $\boldsymbol{x}_0$ and set to zero, which yields the normal equation

$$\hat{x}_0 = \left(\sum \mathbf{H^T W H} + \bar{P}_0^{-1}\right)^{-1} \left(\sum \mathbf{H^T W y} + \bar{P}_0^{-1}\bar{\boldsymbol{x}}_0\right), \tag{34}$$

where $\hat{x}_0$ denotes the correction to the full state, bold quantities belong to the summation notation, quantities in the first parenthesis are called the information matrix Λ, and quantities in the second parenthesis are called the normal matrix (N). The covariance matrix (P) that defines the uncertainty of the estimated parameters can be obtained by taking the inverse of the information matrix, as shown in Equation (34).

6. RESULTS

In this section, the solution from the least-squares filter is discussed. The entire data arc from 1992 through 2008 was fit simultaneously instead of fitting two consecutive apparitions and adding more data for the next observation arc. Although the angular velocity data is available, only the Euler angles were processed. The angular velocity data was used to validate that the filter solution accurately models the stated spin state of Toutatis. One difficulty encountered during the estimation process is that when the actual observation uncertainties were used to weight the data, the filter did not converge. Thus, the observation uncertainties were artificially inflated to ensure convergence. The observation uncertainties were uniformly increased to 15 deg for the 1992 through 2000 apparitions and 20 deg for the 2004 through 2008 apparitions.

The initial conditions (i.e., reference state), 1σ a priori uncertainties, converged solution, and estimated 1σ uncertainties of Toutatis' spin state at 17:49:47 UTC on 1992 November 9 are presented in Table 2.

The initial Euler angles and angular velocity were obtained by backward propagation of one of the observations during the 1992 flyby. This particular epoch was chosen because it is one month prior to Toutatis' closest approach to the Earth during the 1992 apparition, and it coincides with the onset of the terrestrial torque for this data arc. As mentioned above, the moments of inertia are all normalized by I_{zz}. For a qualitative analysis, it is only necessary to know the ratios of the moments of inertia to infer the internal structure of the body. These moment of inertia ratios were estimated by coauthor Busch starting from the solution of Ostro et al. (1999). Note that the uncertainty of I_{zz} is tightened so the filter practically leaves this parameter out of the state vector (i.e., I_{zz} is not a free parameter as the moment of inertia ratios are estimated).

The converged solution shows that the off-diagonal terms in the inertia tensor and the COM-COF offset are indistinguishable from zero. Also, the Euler angles, diagonal terms of the inertia tensor, and COM-COF offset have far lower uncertainties compared to the a priori uncertainties. The uncertainties of the angular velocity would decrease further had they been included in the observations; instead, the angular velocity data are used to validate the estimated solution. Figure 7 shows the Euler angle post-fit residuals normalized by the observation uncertainties.

In Figure 7, all post-fit residuals lie within the 3σ bounds. One observation during the 1992 apparition was recorded when Toutatis was observed nearly end-on, and it corresponds to the largest post-fit residual near the -3σ bounds (i.e., a diamond marker). Figure 8 shows the normalized angular velocity residuals for the converged solution.

Table 2
Initial Condition and Converged Solution of the State Vector and Their Uncertainties at 17:49:47 UTC on 1992 November 9

Parameter	Initial Value	A Priori 1σ Uncertainty	Estimated Value	Estimated 1σ Uncertainty
α (deg)	144.863	15	145.498	3.762
β (deg)	65.467	15	65.865	2.388
γ (deg)	241.785	15	241.524	2.586
ω_1 (deg day^{-1})	14.514	0.1	14.510	0.0994
ω_2 (deg day^{-1})	33.532	0.1	33.529	0.0971
ω_3 (deg day^{-1})	−98.713	0.1	−98.709	0.0957
$\bar{I}_{xx}$ (n.d.)	3.091	1×10^{-1}	3.0836	0.02822
$\bar{I}_{yy}$ (n.d.)	3.2178	1×10^{-1}	3.235	0.0714
$\bar{I}_{zz}$ (n.d.)	1	1×10^{-9}	1	1×10^{-9}
$\bar{I}_{xy}$ (n.d.)	0	1×10^{-2}	-7.1082×10^{-4}	0.00994
$\bar{I}_{yz}$ (n.d.)	0	1×10^{-2}	1.1707×10^{-3}	0.00939
$\bar{I}_{xz}$ (n.d.)	0	1×10^{-2}	1.3252×10^{-3}	0.00753
$\bar{r}_x$ (km)	0	1×10^{-3}	5.126×10^{-7}	1.6789×10^{-5}
$\bar{r}_y$ (km)	0	1×10^{-3}	-1.720×10^{-7}	3.3489×10^{-5}
$\bar{r}_z$ (km)	0	1×10^{-3}	-3.6732×10^{-7}	4.2864×10^{-5}

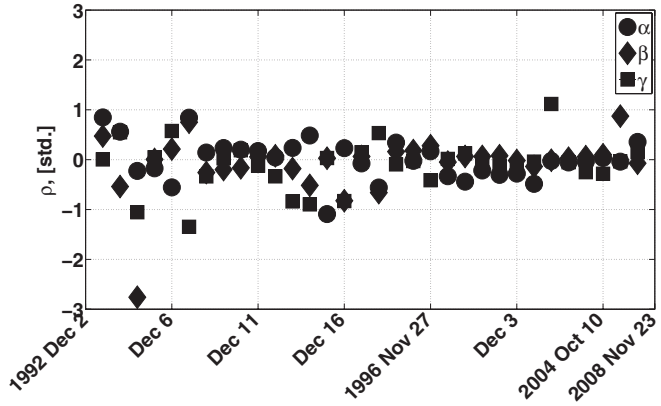

Figure 7. Euler angle post-fit residuals normalized by observation uncertainties. The circle markers are the first Euler angle, the diamond markers are the second, and the square markers are the third.

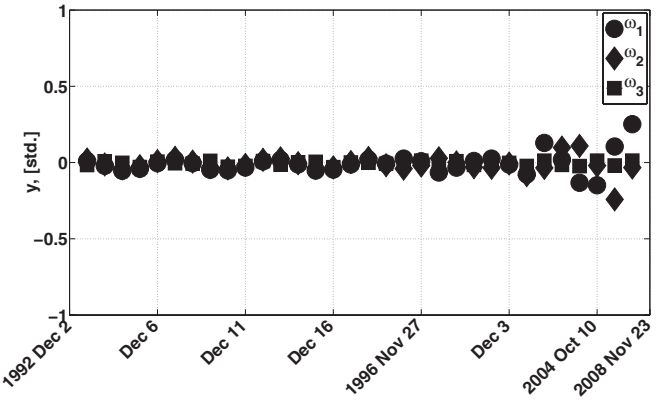

Figure 8. Angular velocity post-fit residuals normalized by observation uncertainties. The circle markers are the first components, the diamond markers are the second components, and the square markers are the third components of the angular velocity.

As shown in Figure 8, none of the observations exceed the 3σ bounds, or even 1σ bounds, and the angular velocity is well modeled by the converged solution.

7. DISCUSSIONS AND FUTURE OBSERVATION OPPORTUNITIES

The moment of inertia ratios I_{xx}/I_{zz} and I_{yy}/I_{zz} are estimated to a fractional precision of 0.9% and 2.2%, respectively. These measurements are unprecedented for any near-Earth asteroid, and will provide stringent constraints on Toutatis' internal density distribution. However, it is still inappropriate to make any claims to the absence or presence of internal density variations at this time, because the current Toutatis shape model is not sufficiently accurate to distinguish mass anomalies of <3% of the asteroid's total mass from shape differences. The radar and Chang'e 2 images from 2012 show that the shape model of Hudson et al. (2003) only corresponds to Toutatis' actual shape over ∼97% of its volume. When a more accurate shape model of Toutatis is available, the moment ratio measurements will be sensitive to smaller mass anomalies.

Using the converged solution provided in Table 2, we extrapolated our model of Toutatis' spin state forward in time from 2008 to Toutatis' next Earth flybys in 2012 December and 2016 December/2017 January. The uncertainties in Toutatis' predicted orientation grow with time; during the 2012 flyby, they were ∼25 deg (3σ). With that caveat, we predicted what we would see during future radar imaging campaigns.

During the 2012 flyby, over December 3–22, Goldstone obtained delay-Doppler resolution as fine as 0.025 μs delay/3.75 m range resolution (closest approach was 0.04633 AU on 2012 December 12). As viewed from Earth, Toutatis was seen from both broadsides (sub-Earth point near the $+z$ and $-z$ directions) and both ends (sub-Earth near the $+x$ and $-x$ directions), showing nearly the entire surface. The asteroid's orientations matched our predictions to within their uncertainties. Following the radar campaign, we have begun to refine our spin state model to match Toutatis' orientation in 2012 to within a few degrees and to match the spin vector measurements from radar speckle tracking (Busch et al. 2009). We will then be able to make a better comparison between our model and images from the Chang'e 2 flyby. The final results of the 2012 radar campaign will be the subject of a future paper.

At the end of 2016 and the beginning of 2017, Toutatis will be much farther from the Earth than in 2012 (0.2512 AU on

2016 December 29). Radar observations would be limited to Arecibo only, with a delay resolution of ~1 μs or 300 m in range, which would still be sufficient to improve the spin state model, measuring the spin state change from the 2012 flyby. There will be no significant tidal torques from the Earth due to the 2016 flyby, because of the greater distance. After 2016, Toutatis will not approach within 0.5 AU of Earth until 2065, when it begins the next set of once-per-four-years flybys, and there will be no additional radar opportunities until then. There will be frequent opportunities for optical light-curve observations, which would further improve our knowledge of Toutatis' spin state.

8. CONCLUSIONS

In this paper, a method to estimate the rotational dynamics of a tumbling body was described. Specifically, this method was applied to estimate the rotational dynamics of 4179 Toutatis, which is a near-Earth asteroid that has been making an Earth flyby approximately every four years. The spin state estimation was realized by directly relating the COM-COF offset and the moment of inertia ratios to the spherical harmonic coefficients of the first- and second-degree gravity potential, which is the driving force of the external torque due to an external spherical body. The dynamical model included the solar and terrestrial torques as perturbations. The Euler angle data between 1992 and 2008 obtained at Goldstone and Arecibo were processed to show that the asteroid has a negligible COM-COF offset, and that the estimated moment of inertia ratios predicted Toutatis' 2012 December orientation within the formal uncertainties of 20–30 deg. In the future, the 2012 observations will be used to refine the spin state model and compare it to an improved Toutatis shape model to constrain the asteroid's internal structure.

Funding was provided by JPL and radar imaging was provided by Goldstone, Arecibo, and VLA. D.J.S. and Y.T. were supported by NASA grants NNX09AU23G and NNX10AG53G from the Outer Planets Research and Near-Earth Object Observation Programs, respectively. M.W. Busch was partially supported by the National Radio Astronomy Observatory's Jansky Postdoctoral Fellowship program.

Facilities: Arecibo, GSSR, VLA

APPENDIX

APPENDIX MATERIAL

A.1. Dynamics Matrix

In order to compute the STM, it is necessary to compute the dynamics matrix A (Equation (32)). There are only five components that are nonzero in the dynamics matrix, which are $\partial\dot{\boldsymbol{\alpha}}/\partial\boldsymbol{\alpha}$, $\partial\dot{\boldsymbol{\alpha}}/\partial\boldsymbol{\omega}$, $\partial\dot{\boldsymbol{\omega}}/\partial\boldsymbol{\omega}$, $\partial\dot{\boldsymbol{\omega}}/\partial I_{ij}$, and $\partial\dot{\boldsymbol{\omega}}/\partial\boldsymbol{r}_{\rm CM}$. These five quantities are solved below.

A.1.1. $\partial\dot{\boldsymbol{\alpha}}/\partial\boldsymbol{\alpha}$

From Equation (4), $\partial\dot{\boldsymbol{\alpha}}/\partial\boldsymbol{\alpha}$ is computed as

$$\frac{\partial\dot{\boldsymbol{\alpha}}}{\partial\alpha} = \frac{\partial[C(\boldsymbol{\alpha})]}{\partial\alpha}\boldsymbol{\omega}_B = 0; \tag{A1}$$

$$\frac{\partial\dot{\boldsymbol{\alpha}}}{\partial\beta} = \frac{\partial[C(\boldsymbol{\alpha})]}{\partial\beta}\boldsymbol{\omega}_B = \frac{1}{\sin^2\beta}\begin{bmatrix} -\sin\gamma\cos\beta & -\cos\gamma\cos\beta & 0 \\ 0 & 0 & 0 \\ \sin\gamma & \cos\gamma & 0 \end{bmatrix}\boldsymbol{\omega}_B; \tag{A2}$$

$$\frac{\partial\dot{\boldsymbol{\alpha}}}{\partial\gamma} = \frac{\partial[C(\boldsymbol{\alpha})]}{\partial\gamma}\boldsymbol{\omega}_B = \begin{bmatrix} \dfrac{\cos\gamma}{\sin\beta} & -\dfrac{\sin\gamma}{\sin\beta} & 0 \\ -\sin\gamma & -\cos\gamma & 0 \\ -\dfrac{\cos\gamma}{\tan\beta} & \dfrac{\sin\gamma}{\tan\beta} & 0 \end{bmatrix}\boldsymbol{\omega}_B. \tag{A3}$$

A.1.2. $\partial\dot{\boldsymbol{\alpha}}/\partial\boldsymbol{\omega}$

Also from Equation (4), $\partial\dot{\boldsymbol{\alpha}}/\partial\boldsymbol{\omega}$ is computed as

$$\frac{\partial\dot{\boldsymbol{\alpha}}}{\partial\omega} = [C(\boldsymbol{\alpha})]. \tag{A4}$$

A.1.3. $\partial\dot{\boldsymbol{\omega}}/\partial\boldsymbol{\omega}$

First, note the following identity:

$$\frac{\partial(\tilde{\omega}\boldsymbol{a})}{\partial\boldsymbol{\omega}} = \frac{\partial(\boldsymbol{\omega}\times\boldsymbol{a})}{\partial\boldsymbol{\omega}} = -\frac{\partial(\boldsymbol{a}\times\boldsymbol{\omega})}{\partial\boldsymbol{\omega}} = -\frac{\partial(\tilde{a}\boldsymbol{\omega})}{\partial\boldsymbol{\omega}} = -\tilde{a}. \tag{A5}$$

Then, from Equation (8), $\partial\dot{\boldsymbol{\omega}}/\partial\boldsymbol{\omega}$ becomes

$$\frac{\partial\dot{\boldsymbol{\omega}}_{B,\rm CM}}{\partial\boldsymbol{\omega}_{B,\rm CM}} = I_{B,\rm CM}^{-1}\left([\tilde{I\boldsymbol{\omega}}]_{B,\rm CM} - \tilde{\omega}_{B,\rm CM}I_{B,\rm CM} + \frac{\partial\boldsymbol{L}_{B,\rm CM}}{\partial\boldsymbol{\omega}_{B,\rm CM}}\right), \tag{A6}$$

where $\partial\boldsymbol{L}_{B,\rm CM}/\partial\boldsymbol{\omega}_{B,\rm CM}$ is nominally a zero matrix.

A.1.4. $\partial\dot{\boldsymbol{\omega}}/\partial I_{ij}$

From Equation (8), the partial of $\dot{\boldsymbol{\omega}}$ with respect to I_{ij} is computed as

$$\frac{\partial\dot{\boldsymbol{\omega}}}{\partial I_{ij}} = \frac{\partial(I^{-1})}{\partial I_{ij}}(-\tilde{\omega}I\boldsymbol{\omega}+\boldsymbol{L}) + I^{-1}\left(-\tilde{\omega}\frac{\partial I}{\partial I_{ij}}\boldsymbol{\omega} + \frac{\partial\boldsymbol{L}}{\partial I_{ij}}\right). \tag{A7}$$

In order to compute $\partial(I^{-1})/\partial I_{ij}$, the familiar identity $I^{-1}I = 1_{[3\times3]}$ becomes useful. That is,

$$\frac{\partial(I^{-1}I)}{\partial I_{ij}} = \frac{\partial(I^{-1})}{\partial I_{ij}}I + I^{-1}\frac{\partial I}{\partial I_{ij}} = \boldsymbol{0}, \tag{A8}$$

which yields

$$\frac{\partial(I^{-1})}{\partial I_{ij}} = -I^{-1}\frac{\partial I}{\partial I_{ij}}I^{-1}. \tag{A9}$$

Thus, Equation (A7) becomes

$$\frac{\partial\dot{\boldsymbol{\omega}}}{\partial I_{ij}} = -I^{-1}\frac{\partial I}{\partial I_{ij}}I^{-1}(-\tilde{\omega}I\boldsymbol{\omega}+\boldsymbol{L}) + I^{-1} \times\left(-\tilde{\omega}\frac{\partial I}{\partial I_{ij}}\boldsymbol{\omega} + \frac{\partial\boldsymbol{L}}{\partial I_{ij}}\right). \tag{A10}$$

Note that $\boldsymbol{L}$ is expressed as a function of the spherical harmonics. These spherical harmonics are linearly related to the inertia tensor, so the chain rule can be used to compute $\partial\boldsymbol{L}/\partial I_{ij}$. The acceleration due to U_2 (Equation (19)) can be expressed as:

$$\frac{\partial U_2}{\partial\boldsymbol{r}} = \boldsymbol{a}_{C_{20}}C_{20} + \boldsymbol{a}_{C_{21}}C_{21} + \boldsymbol{a}_{C_{22}}C_{22} + \boldsymbol{a}_{S_{21}}S_{21} + \boldsymbol{a}_{S_{22}}S_{22} = \sum\boldsymbol{a}_{C_{2ml}}C_{2ml}, \tag{A11}$$

Table 3
Observation Log

Date	Mid-epoch (UTC)	Resolution (μs × Hz)	Euler Angles (deg)	Angular Velocity (deg day^{-1})
		Goldstone		
1992 Dec 2	21:40	0.500 × 0.1000	(122.2, 86.5, 107.0)	(−35.6, 7.2, −97.0)
1992 Dec 3	19:30	0.500 × 0.1000	(86.3, 81.8, 24.5)	(−16.4, −29.1, −91.9)
1992 Dec 4	18:10	0.500 × 0.1000	(47.8, 60.7, 284.0)	(29.1, −23.2, −97.8)
1992 Dec 5	18:50	0.125 × 0.0833	(14.6, 39.4, 207.1)	(33.3, 8.2, −92.2)
1992 Dec 6	17:30	0.125 × 0.0833	(331.3, 23.7, 151.6)	(6.6, 34.5, −95.8)
1992 Dec 7	17:20	0.500 × 0.1000	(222.5, 25.4, 143.9)	(12.8, 25.4,−104.1)
1992 Dec 8	16:40	0.125 × 0.0330	(169.8, 45.5, 106.9)	(−31.1, −21.9, −97.7)
1992 Dec 9	17:50	0.125 × 0.0330	(137.3, 71.3, 22.3)	(11.8,−36.9, −94.9)
1992 Dec 10	17:20	0.125 × 0.0330	(103.1, 85.2,292.6)	(35.8, −8.9, −97.9)
1992 Dec 11	09:40	0.500 × 0.1000	(77.0, 85.7, 225.5)	(31.0, 17.0, −96.3)
1992 Dec 12	09:20	0.500 × 0.1000	(42.8, 70.2, 133.2)	(−1.3, 37.0, −95.9)
1992 Dec 13	08:10	0.500 × 0.1000	(13.7, 44.4, 51.9)	(−38.3, 17.9, −97.3)
1992 Dec 14	07:50	0.500 × 0.1000	(323.7, 14.0, 0.0)	(−70.5, −30.6, −91.1)
1992 Dec 15	07:50	0.500 × 0.1000	(193.2, 24.4, 21.4)	(22.1,−26.6, −96.6)
1992 Dec 16	07:10	0.500 × 0.1000	(165.1, 46.4, 310.6)	(33.4, −3.4, −93.7)
1992 Dec 17	06:49	0.500 × 0.1000	(130.6, 76.1, 234.9)	(12.6, 33.9,−94.0)
1992 Dec 18	07:09	0.500 × 0.1000	(91.6, 81.6, 142.4)	(−24.3, 29.6, −102.0)
		Goldstone		
1996 Nov 25	19:48	0.125 × 0.0331	(130.5, 78.9, 143.2)	(−32.0, 16.4, −98.2)
1996 Nov 26	17:51	0.125 × 0.0331	(94.2, 88.1, 57.7)	(−30.6, −18.7, −91.5)
1996 Nov 27	17:34	0.125 × 0.0331	(60.4, 81.2, 320.9)	(10.7,−36.8, −94.7)
1996 Nov 29	15:37	0.125 × 0.0331	(349.3, 30.0, 168.0)	(23.1, 28.9, −98.3)
1996 Nov 30	15:47	0.125 × 0.0331	(250.3, 14.2, 166.9)	(−18.6, 32.1, −94.9)
1996 Dec 1	14:23	0.125 × 0.0331	(180.4, 37.6, 139.3)	(−38.7, −0.5, −98.1)
1996 Dec 2	13:43	0.125 × 0.0331	(146.7, 64.0, 64.9)	(−12.6, −34.8, −97.9)
1996 Dec 3	12:20	0.125 × 0.0331	(116.7, 81.4, 340.4)	(24.3,−28.2, −98.1)
		Goldstone		
2000 Nov 4	17:06	0.125 × 0.0331	(110.0, 88.5, 30.0)	(0.0,−32.5, −98.9)
2000 Nov 5	18:01	0.125 × 0.0331	(70.6, 84.0, 281.0)	(34.5,−17.2, −97.9)
		Arecibo		
2004 Oct 7	13:56	0.100 × 0.0114	(79.9, 85.3, 365.2)	(−2.5, −35.4, −109.0)
2004 Oct 8	14:04	0.100 × 0.0114	(44.9, 72.5, 263.1)	(32.4,−18.1, −97.9)
2004 Oct 9	13:57	0.100 × 0.0114	(12.8, 47.3, 181.4)	(29.7, 22.8, −98.1)
2004 Oct 10	13:17	0.100 × 0.0114	(327.7, 20.4, 124.1)	(−10.7, 34.7, −97.3)
		Arecibo		
2008 Nov 22	10:54	0.100 × 0.0186	(119.5, 90.7, 92.0)	(118.1, 90.4, 93.6)
2008 Nov 23	10:45	0.100 × 0.0186	(86.2, 85.0, 0.3)	(−0.4, −36.2, −98.9)

Notes. Toutatis' orientations and instantaneous spin vectors as estimated from Goldstone and Arecibo delay-Doppler images from 1992 to 2008. Times are given at the mid-epoch of each observation and image resolution is given in time delay and Doppler shift.

where each $\boldsymbol{a}$ is the partial of the total acceleration with respect to the parameter in the subscript, and C_{2ml} denotes all second-degree spherical harmonics ordered in the following manner:

$$C_{2ml} = [C_{20} \quad C_{21} \quad C_{22} \quad S_{21} \quad S_{22}]. \tag{A12}$$

Then, the torque due to the second-degree potential is expressed as

$$\boldsymbol{L}_2 = -M_s \boldsymbol{r} \times \frac{\partial U_2}{\partial \boldsymbol{r}} = -M_s[\tilde{r}] \left(\sum \boldsymbol{a}_{C_{2ml}} C_{2ml} \right). \tag{A13}$$

Thus, the partial of the torque due to the second-degree spherical harmonics is given as

$$\frac{\partial \boldsymbol{L}_2}{\partial C_{2ml}} = -M_s[\tilde{r}] \boldsymbol{a}_{C_{2ml}}. \tag{A14}$$

Applying the chain rule, we get

$$\begin{aligned} \frac{\partial \boldsymbol{L}}{\partial I_{xx}} &= \frac{\partial \boldsymbol{L}}{\partial C_{20}} \frac{\partial C_{20}}{\partial I_{xx}} + \frac{\partial \boldsymbol{L}}{\partial C_{22}} \frac{\partial C_{22}}{\partial I_{xx}} \\ &= -\frac{GM_s}{M^*(R^*)^2} [\tilde{r}] \left(\frac{1}{2} \boldsymbol{a}_{C_{20}} - \frac{1}{4} \boldsymbol{a}_{C_{22}} \right); \end{aligned} \tag{A15}$$

$$\begin{aligned} \frac{\partial \boldsymbol{L}}{\partial I_{yy}} &= \frac{\partial \boldsymbol{L}}{\partial C_{20}} \frac{\partial C_{20}}{\partial I_{yy}} + \frac{\partial \boldsymbol{L}}{\partial C_{22}} \frac{\partial C_{22}}{\partial I_{yy}} \\ &= -\frac{GM_s}{M^*(R^*)^2} [\tilde{r}] \left(\frac{1}{2} \boldsymbol{a}_{C_{20}} + \frac{1}{4} \boldsymbol{a}_{C_{22}} \right); \end{aligned} \tag{A16}$$

$$\frac{\partial \boldsymbol{L}}{\partial I_{zz}} = \frac{\partial \boldsymbol{L}}{\partial C_{20}} \frac{\partial C_{20}}{\partial I_{zz}} = \frac{GM_s}{M^*(R^*)^2} [\tilde{r}] \boldsymbol{a}_{C_{20}}; \tag{A17}$$

$$\frac{\partial \boldsymbol{L}}{\partial I_{xy}} = \frac{\partial \boldsymbol{L}}{\partial S_{22}} \frac{\partial S_{22}}{\partial I_{xy}} = \frac{GM_s}{2M^*(R^*)^2} [\tilde{r}] \boldsymbol{a}_{S_{22}}; \tag{A18}$$

$$\frac{\partial \boldsymbol{L}}{\partial I_{yz}} = \frac{\partial \boldsymbol{L}}{\partial S_{21}} \frac{\partial S_{21}}{\partial I_{yz}} = \frac{GM_s}{M^*(R^*)^2} [\tilde{r}] \boldsymbol{a}_{S_{21}}; \tag{A19}$$

$$\frac{\partial \boldsymbol{L}}{\partial I_{xz}} = \frac{\partial \boldsymbol{L}}{\partial C_{21}} \frac{\partial C_{21}}{\partial I_{xz}} = \frac{GM_s}{M^*(R^*)^2} [\tilde{r}] \boldsymbol{a}_{C_{21}}. \tag{A20}$$

A.1.5. $\partial \dot{\boldsymbol{\omega}} / \partial \boldsymbol{r}_{\mathrm{CM}}$

From Equation (8), the partial of $\dot{\boldsymbol{\omega}}$ with respect to $\boldsymbol{r}_{\mathrm{CM}}$ is computed as

$$\frac{\partial \dot{\boldsymbol{\omega}}}{\partial \boldsymbol{r}_{\mathrm{CM}}} = I^{-1} \left(\sum_{\mathrm{Earth,Sun}} \frac{\partial \boldsymbol{L}_1}{\partial \boldsymbol{r}_{\mathrm{CM}}} \right), \tag{A21}$$

where the following equation is substituted:

$$\frac{\partial \boldsymbol{L}_1}{\partial \boldsymbol{r}_{\mathrm{CM}}} = -\frac{GM^* M_s}{r^3} [\tilde{r}]. \tag{A22}$$

A.2. Observation Log

Table 3 lists the observations of Toutatis used in our least-squares filter and radar images recorded at Goldstone between 1992 and 2000 and at Arecibo between 2004 and 2008. Additional radar images were obtained at Arecibo in 1992 (Ostro et al. 1995; Hudson & Ostro 1995), but these overlapped the time span of the Goldstone observations and do not provide more information on the spin state.

REFERENCES

Busch, M. W., Kulkarni, S. R., Brisken, W., et al. 2009, Icar, 209, 535
Danby, J. M. A. 1962, Fundamentals of Celestial Mechanics (2nd ed.; Richmond, VA: Willman-Bell, Inc.)
Hudson, R. S., & Ostro, S. J. 1995, Sci, 270, 84
Hudson, R. S., & Ostro, S. J. 1998, Icar, 135, 451
Hudson, R. S., Ostro, S. J., & Scheeres, D. J. 2003, Icar, 161, 346
Ostro, S. J., Hudson, R. S., Jurgens, R. F., et al. 1995, Sci, 270, 80
Ostro, S. J., Hudson, R. S., Rosema, K. D., et al. 1999, Icar, 137, 122
Schaub, H., & Junkins, J. L. 2009, Analytical Mechanics of Space Systems (2nd ed.; Reston, VA: American Institute of Aeronautics and Astronautics, Inc.)
Scheeres, D. J., Ostro, S. J., Werner, R. A., Asphaug, E., & Hudson, R. S. 2000, Icar, 147, 106
Spencer, J. R., Akimov, L. A., Angeli, C., et al. 1995, Icar, 117, 71
Tapley, B. D., Schutz, B. E., & Born, G. H. 2004, Statistical Orbit Determination (Philadelphia, PA: Elsevier Academic Press)